Hybrid monometallic and bimetallic copper–palladium zeolite catalysts for direct synthesis of dimethyl ether from CO 2

Sara Navarro-Jaén, Mirella Virginie, Jean-Charles Morin, Joëlle Thuriot-Roukos, Robert Wojcieszak, Andrei Khodakov

January 12th, 2022

Hybrid monometallic and bimetallic copper-palladium zeolite catalysts for direct synthesis of dimethyl ether from CO_2

*Sara Navarro-Jaén, Mirella Virginie, Jean-Charles Morin, Joëlle Thuriot-Roukos, Robert Wojcieszak and Andrei Y. Khodakov**

Univ. Lille, CNRS, Centrale Lille, ENSCL, Univ. Artois, UMR 8181 – UCCS – Unité de Catalyse et Chimie du Solide, F-59000 Lille, France

**Corresponding author: *andrei.khodakov@univ-lille.fr*; Tel.: +33 3 20 33 54 39

Abstract

Nowadays, carbon dioxide is the major reason of the global climate changes. The direct CO_2 hydrogenation to dimethyl ether produces an important platform molecule for synthesis of fuels and chemicals and at the same time, utilizes large amounts of this greenhouse gas. In this paper, we prepared a series of hybrid catalysts, which are composed by alumina supported copper-palladium nanoparticles and HZSM-5 zeolite for direct synthesis of dimethyl ether from CO_2. Copper active sites showed higher intrinsic activity for CO_2 hydrogenation compared to palladium. Low palladium content in the copper-palladium bimetallic catalysts was particularly beneficial for the dimethyl ether production. Undesirable methane and ethane productions were completely suppressed, while the dimethyl ether selectivity has considerably increased. Extensive catalyst characterization combined with catalytic measurements was indicative of the presence of copper and palladium monometallic and bimetallic particles with different size and reducibility in the hybrid catalysts. The presence of even small amounts of palladium significantly improved copper reducibility and copper dispersion. Some decrease in the Brønsted acidity in the copper containing catalysts was due to the migration of unreduced copper ions in the zeolite channels during the reduction. The methanol dehydration to dimethyl ether was only slightly affected by the amounts of Brønsted acid sites in the hybrid catalysts.

Keywords: Carbon dioxide; hydrogenation; dimethyl ether; methanol; hybrid catalysts

1. Introduction

Nowadays, carbon dioxide is the most important industrial pollutant and is also the major reason of the global climate changes. Rapidly growing CO_2 concentration in the atmosphere can be addressed on the one hand, by reducing the CO_2 emission from human activities and on the other hand, by carbon dioxide removal from the atmosphere, using carbon capture and storage (CCS)[1] and carbon capture and utilization (CCU) [2]. In the carbon capture and utilization strategy[2–5], CO_2 is converted to fuels and chemicals using biological, thermo-catalytic, electrocatalytic and photocatalytic routes. Dimethyl ether (DME)[6–8] is one of the most promising environmentally optimized alternatives to the conventional fossil fuels (gasoline or diesel fuels) due to its high cetane index (> 55), low emission of CO, NOx, particulates and reduced noise. DME can be also used as a substitute for liquefied petroleum gas (LPG) that is widely used as fuel in industry and household. DME is biodegradable in air, non-cancerogenic and non-corrosive. In addition, DME is an important intermediate for the production of useful chemicals (i.e. methyl acetate and dimethyl sulfate) and petrochemicals (light olefins, BTX aromatics). In the industry, DME is currently produced from syngas (carbon monoxide and hydrogen) via direct and indirect routes [6–10] from various feedstocks like natural/shale gas, coal, oil or biomass. Most of previous publications on CO_2 hydrogenation have addressed [5] methanol synthesis. Copper catalysts (often containing zinc) and palladium have been shown [6,11–16] good activity in the methanol synthesis from both CO and CO_2. Jiang [17] et al observed a strong promoting synergistic effect on the methanol formation over amorphous silica supported Pd–Cu bimetallic catalysts, when the Pd/(Pd + Cu) atomic ratios lied in the range of 0.25–0.34.

Different to the methanol synthesis, direct DME production from CO_2 requires bifunctional catalysts containing a function for the CO_2 selective hydrogenation to methanol (Eq. 1) and an acid function for the methanol dehydration (Eq. 2)[18]:

$$CO_2+3H_2 \leftrightarrow CH_3OH + H_2O \qquad \Delta H^0_{298}=-49.3 \text{ kJ/mol} \qquad \text{(Eq. 1)}$$

$2\ CH_3OH \leftrightarrow CH_3OCH_3+H_2O$ $\Delta H^0_{298}=-24.0$ kJ/mol (Eq. 2)

$CO_2+H_2 \leftrightarrow CO + H_2O$ $\Delta H^0_{298}= 41.2$ kJ/mol (Eq. 3)

$CO_2+4H_2 \leftrightarrow CH_4 + 2H_2O$ $\Delta H^0_{298}= -165.0$ kJ/mol (Eq. 4)

The DME production is usually conditioned by the rate of methanol formation [19] in the proximity of the metal-oxide interface, followed by a rapid transfer of methanol towards neighboring acid sites of the zeolite. The interaction between metal and acid functions[20,21] can strongly affect the activity and selectivity. The DME yield can further enhanced by process intensification including membrane reactor technology[22–24] and sorption-enhanced dimethyl ether synthesis (SEDMES) [25]. The main side reactions of the CO_2 hydrogenation are the reverse water gas shift (RWGS, Eq. 3) and methanation (Eq. 4).

One of major challenges of the direct DME synthesis from CO_2 is possible presence of methane and light alkanes in the reaction products. Methane and light alkanes cannot be converted to DME under the process conditions, different to CO and methanol. Another challenge of direct DME synthesis from CO_2 is insufficient stability of bifunctional catalysts. Indeed, metal nanoparticles may undergo sintering[26–28] and oxidation[28]. The presence of strong acid sites in the catalysts is not desirable, since these sites can lead to the formation of olefins and coke deposition. A particular attention should be therefore paid[6] to the localization and synergy of metallic and acid functions in the bifunctional catalysts. The ZSM-5 zeolite has often been used as the acid component in bifunctional DME synthesis catalysts. The zeolite based catalysts have several advantages[29] for methanol dehydration to DME in respect to more conventional alumina such as tunable acidity and better stability in the presence of steam [30].

The present manuscript addresses design of hybrid bifunctional catalysts on the basis of supported copper-palladium monometallic and bimetallic particles supported on alumina and ZSM-5 zeolite for direct synthesis of DME from CO_2. To the best of our knowledge, no previous publications have addressed direct synthesis of DME using CO_2 hydrogenation over

hybrid Pd-Cu catalysts. Our goal was to elucidate the role of copper and palladium in bimetallic catalysts on the catalyst structure, CO_2 conversion, DME production rate, reaction selectivity and catalyst stability. The catalyst characterization using the XRD, TPR, XPS, STEM-EDX, FTIR techniques was combined with catalytic measurements in a high-pressure catalytic reactor.

2. Experimental

2.1. Catalyst synthesis

Copper (II) acetate (Sigma-Aldrich, 98%), tetraamminepalladium (II) nitrate aqueous solution (10 wt.% metal content, Sigma-Aldrich) and commercial high surface area γ-Al_2O_3 (Riogen, > 98%) were used as raw materials for synthesis of the bimetallic PdCu/Al_2O_3 catalysts. The PdCu/Al_2O_3 catalysts with 7 wt.% Cu nominal content and different Pd loadings (2, 4 and 6 wt.%) were prepared by co-impregnation. For that purpose, 25 mL of a 0.27 M copper acetate aqueous solution ($C_4H_6CuO_4$) were prepared and kept under stirring for 10 minutes. The γ-Al_2O_3 support was then added, and the mixture was stirred for 1 h. Subsequently, 25 mL of an aqueous solution containing the appropriate amounts of $Pd(NH_3)_4(NO_3)_2$ were added dropwise and the mixture was kept under stirring for 1 h. Afterwards, the obtained solid was dried overnight at 100 °C and calcined at 350 °C for 4 h with a heating rate of 2 °C·min^{-1}. The resulting catalysts were labelled as 2PdCuAl, 4PdCuAl and 6PdCuAl. For the sake of comparison, 7 wt.% Cu/Al_2O_3 and 6 wt.% Pd/Al_2O_3 monometallic catalysts, namely CuAl and PdAl respectively, were also prepared.

A powder of the ammonium form of ZSM-5 zeolite with SiO_2/Al_2O_3 ratio of 23 (CVB 2314, Zeolyst) was used as precursor for the preparation of the H-ZSM-5 acid catalyst. The latter, referred in the present manuscript as Z, was obtained by calcination of the ammonium form at 550 °C for 6 h at a heating rate of 2 °C·min^{-1}.

Finally, the hybrid MAl//Z (M=Cu, Pd or PdCu) catalysts with a 5:1 mass ratio were prepared by mechanical mixing of the mono- or bimetallic catalysts and ZSM-5 zeolite in an agate mortar. An appropriate quantity of the as prepared M-Al catalyst was put in the mortar with the corresponding Z zeolite (ratio 5:1). The catalysts were manually mixed during 10 min at room temperature to obtain a homogeneous mixture. The as-prepared sample was used for the catalytic tests after H_2 activation.

2.2. Catalyst characterization

The elemental analysis of the bimetallic catalysts was performed by Inductively Coupled Plasma-Optic Emission Spectroscopy (ICP-OES) after acid digestion in a HNO_3/HF mixture. The measurements were performed in a 720-ES ICP-OES (Agilent) spectrometer, with axial view and simultaneous CCD detection. The software ICP Expert^{TM} (version 2.0.4) was used to estimate the weight percentage of each element in the samples.

The powder X-ray diffraction (XRD) patterns were recorded on a Bruker D8 Advance diffractometer using CuKα radiation (λ=1.5406 Å) over the 2 Theta range between 20 and 70° with a step size of 0.01° and a step time of 5 s. The crystallite size of the metallic species was calculated using the Scherrer equation (Eq. 4):

$$\zeta = K\lambda/\beta\cos\theta \qquad \text{(Eq.5)}$$

where ζ is the crystallite size, K is the shape factor, λ is the X-ray wavelength, β is the corrected line broadening at half-maximum intensity and θ is the Bragg angle at the peak position.

The N_2 physisorption experiments at -196°C were performed in a Micromeritics TriStar II Plus apparatus. Prior to the measurements, the samples were degassed at 130 °C for 2 h under vacuum.

The H_2 temperature-programmed reduction (H_2-TPR, 5% H_2 in Ar) was carried out using the AutoChem II 2920 apparatus (Micromeritics). The temperature was increased from 50 ºC to

900 ºC with a heating rate of 10 ºC min^{-1}. The catalyst (20 mg) was exposed to 50 $cm^3 \cdot min^{-1}$ of H_2 5% v/v in Ar, and the temperature was raised from room temperature to 900 °C with a heating rate of 10 °C·min^{-1}.

The X- ray photoelectron spectroscopy (XPS) analyses were performed on a Kratos Axis Ultra DLD spectrometer with a monochromatized Al X-ray source (1486.6 eV) working at 180 W. The spectra of the catalysts were acquired in air at room temperature and after a reduction treatment under H_2 at 350 °C for 1 h. The spectra of samples were referenced to the C 1s signal at 284.8 eV, corresponding to adventitious carbon. The relative surface atomic quantification was performed after the removal of a Shirley type background on each spectrum.

Transmission electron microscopy (TEM) and energy-dispersive X-ray spectroscopy (EDS) measurements were performed on FEI Titan Themis 60-300 kV. The sample was deposited onto a 400-mesh carbon-coated nickel grid. The FEI TITAN Themis 300 Transmission Electron Microscope is equipped with a high-brightness Schottky-type (FEG) field effect source (XFEG) with a monochromator for final energy resolution (0.2 eV). It has an adjustable acceleration voltage from 60 kV to 300 kV and a spherical Cs aberration corrector on the probe (DCOR) for high resolution images in STEM mode (<70 pm). The FEI TITAN microscope also features a high-resolution objective lens (S-TWIN) with a 5.4 mm distance between the polar parts that offers a 70-degree tilt angle with a tomographic specimen holder, CompuStage with a piezo stage for excellent sample holder stability, EDX Super-X detector with superior sensitivity for very fast chemical mapping and four SDD detectors are integrated into the objective lens (S-TWIN). In addition to a high-resolution post-column GATAN energy filter (Quantum ERS / 966) with a system, the equipment with Dual EELS for simultaneous acquisition of low and high energy losses, a CETA 16M camera for a wide field of view of the Image. A three-axis tomographic sample holder (HATA) is also available.

The pyridine (Py) adsorption experiments followed by Fourier-Transform Infrared Spectroscopy (FTIR) were performed using a Thermo Nicolet 460 Protege instrument equipped with a CsI beam splitter and an MCT detector, averaging 256 scans with a 2 cm^{-1} resolution within the 4000-400 cm^{-1} range. The samples were pressed (1000 kg/cm^2) into a self-supported wafer (2.01 cm^2, 10 $mg.cm^{-2}$) and placed in a quartz sample holder in order to align the pellet with respect to the IR beam during the measurements and inserted into a furnace for thermal treatments. The sample holder was then placed in a quartz cell equipped with KBr windows, connected to a vacuum line for evacuation ($P_{residual} \simeq 10^{-6}$ Torr). Prior to the Py adsorption experiments, the samples were reduced at 350 °C under 50 mbar of pure hydrogen and the gas was evacuated under high vacuum ($P_{residual} \simeq 10^{-6}$ Torr) overnight. The Py adsorption was carried out at the equilibrium (1.2 mbar) at 100 °C. The weakly adsorbed Py was then evacuated under high vacuum ($P_{residual} \simeq 10^{-6}$ Torr) at 150°C.

2.3. Catalytic tests

The catalytic performance of the hybrid catalysts in the direct CO_2 hydrogenation was evaluated in a tubular fixed-bed reactor (i. d. 1.4 mm) with the plug flow hydrodynamics operating at 20 bar and 260 °C. We have chosen 260°C taking into account thermodynamic limitations of the reaction. At lower temperatures, the CO_2 conversion is too low, while at higher temperatures, methanation and RWGS are favored [31]. In a typical experiment, 100 mg of the powder catalyst (125< $Ø_p$ <150 μm) were diluted with SiC. Prior to the reaction, the solids were reduced for 1 h at 350°C at atmospheric pressure under 5 $mL \cdot min^{-1}$ of H_2. After conducting the catalyst reduction in H_2 at 350°C, the reactor temperature was decreased to 200°C. The reactor was purged with H_2/CO gas mixture at atmospheric pressure at 200°C. The pressure was then increased to 20 bar and the flow was switched to the reaction mixture, containing 20% CO_2, 60% H_2 and N_2 as balance. Afterwards, the temperature was increased to

260°C.The reactants and reaction products were analyzed using an on-line gas chromatography data system (Scion 456-GC) fitted with ShinCarbon ST, Rt®-Q-BOND columns, TCD and FID detectors.

The CO_2 conversion (Eq. 5, X_{CO2}) and selectivities (Eq. 6, S_i) were calculated as follows [32]:

$$X_{CO_2}(\%) = \left({(F_{CO_2\ in} - F_{CO_2\ out})} \Big/ {F_{CO_2\ in}} \right) \cdot 100 \qquad \text{(Eq.5)}$$

where $F_{CO2\ \mathrm{in}}$ and $F_{CO2\ out}$ are the molar flows of CO_2 at the inlet and the outlet of the reactor, respectively.

$$S_i(\%) = \left({F_i} \Big/ {(F_{CO2\ in} - F_{CO2\ out})} \right) * 100 \qquad \text{(Eq.6)}$$

where F_i refers to the carbon-based molar flow in the product "i" (CO, CH_4, C_2H_6, CH_3OH, DME).

3. Results and discussion

3.1. Catalyst characterization

The physicochemical properties of the studied samples are summarized in **Table 1**. The Z acid catalyst presents a type I (Langmuir) adsorption isotherm at low P/P_o values, indicating the filling of micropores. At higher P/P_o values, the adsorption isotherm is influenced by filling the spaces between the zeolite agglomerates [33]. The hybrid catalysts exhibit type IV(a) adsorption-desorption isotherms and H1-type hysteresis, according to the IUPAC classification, typical of ordered mesoporous materials with uniform cylindrical pores or three-dimensional pore networks [34] (**Fig. S1, Electronic Supplementary Information (ESI)**). The catalysts present specific surface areas ranging from 179.70 to 208.72 $m^2 \cdot g^{-1}$, being their textural properties mainly governed by those of the γ-Al_2O_3 support. Both the Pd and Cu monometallic catalysts display higher specific surface areas than their bimetallic counterparts, which could be explained by lower total metal loading. The metal contents in the catalysts measured by ICP

are close to the nominal values in all catalysts, except in the 6PdCuAl one, in which a loss of Pd has taken place during the synthesis.

Table 1. Structure and composition of metal-zeolite hybrid catalysts (calcined samples)

Sample	S_{BET}, m^2/g	Pd content (wt.%)[a]	Cu content (wt.%)[a]	Pd/Cu atomic ratio	Metal particle size from TEM, nm	Number of Bronsted acid sites, µmol/g	Number of Lewis acid sites, µmol/g	H/M ratio from TPR[c]
γ-Al_2O_3	207.5	-	-	-	-			
Z	155.9	-	-	-	-	99[b]	14[b]	
CuAl//Z	208.6	-	7.0	0	39.0	29	113	2
PdAl//Z	204.4	5.4	-	-	2.8	121	194	1.88
2PdCuAl//Z	179.7	1.9	6.9	0.17	11.4	55	136	1.78
4PdCuAl//Z	208.7	3.3	6.2	0.30	4.2	39	108	1.48
6PdCuAl//Z	189.2	4.1	6.4	0.39	6.0	46	86	1.69

[a] Metal contents determined in the γ-Al_2O_3 supported catalysts before mixing with the Z acid catalyst

[b] Number of Bronsted and Lewis acid sites corresponds to 0.166 g of the HZSM-5 zeolite. This amount relates to the fraction of HZSM-5 zeolite in the hybrid metal zeolite catalysts

[c] Ratio of hydrogen consumption calculated to metal amount in the mono- and bimetallic catalysts calculated from TPR data.

The XRD patterns of the monometallic and bimetallic catalysts are shown in **Fig. 1**. The diffraction pattern of the Z acid catalyst corresponds to a H-ZSM-5 zeolite with a high degree of crystallinity, whereas the support diffractogram corresponds to that of γ-Al_2O_3 (JCPDS-ICDD 00-010-0425). Besides the support XRD patterns, intense diffraction lines associated to

CuO (JCPDS-ICDD 00-041-0254) and Cu_2O (JCPDS-ICDD 00-005-0667) are observed in the diffraction patterns of the CuAl catalyst.

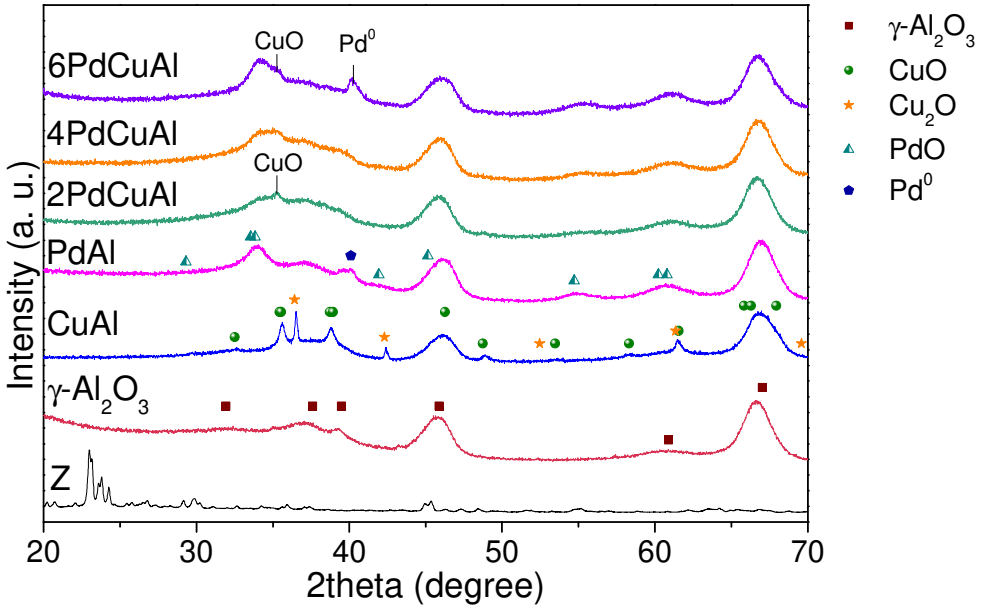

Fig. 1. XRD patterns of the support (γ-Al_2O_3), acid HZSM-5 catalyst (Z) and mono- and bimetallic catalysts after calcination at 350 °C (calcined samples).

The CuO and Cu_2O crystallite sizes calculated from the peak broadening were 27.5 and 52.6 nm respectively, in the copper monometallic catalyst. In the Pd monometallic catalyst, very broad diffraction peaks corresponding to PdO (JCPDS-ICDD 00-041-1107) and metallic Pd (JCPDS-ICDD 00-005-0681) were observed. Reduction of palladium requires a very low activation energy. Spontaneous reduction of Pd under ambient conditions has been observed in a number of previous publications [35–37]. Very broad XRD patterns indicate high Pd dispersion. The mean crystallite size of Pd species calculated using Scherrer's equation was 4.5 nm.

The diffraction lines attributed to the metal species in the 2PdCuAl and 4PdCuAl bimetallic catalysts are located between those corresponding to the pure Cu and Pd species. This points out to the strong interaction between both metals in these samples and possible formation of a PdCu alloy [38,39] and/or a mixed Pd-Cu oxide. The broadening of the XRD peaks attributed to

metallic species also suggests that the presence of Pd significantly improves Cu dispersion. In 2PdCuAl, in addition to the Cu-Pd mixed oxide species, a diffraction line at 35° indicates the presence of CuO crystallites. On the contrary, an increase in the Pd content in the 6PdCuAl catalyst leads to the appearance of peaks corresponding to CuO and metallic Pd, indicting the presence of separated Pd and Cu phases in the solids with the highest Pd content. Metal nanoparticles are located on the Al_2O_3 as the zeolite was introduced after the metal deposition (via physical mixture as detailed in Experimental).

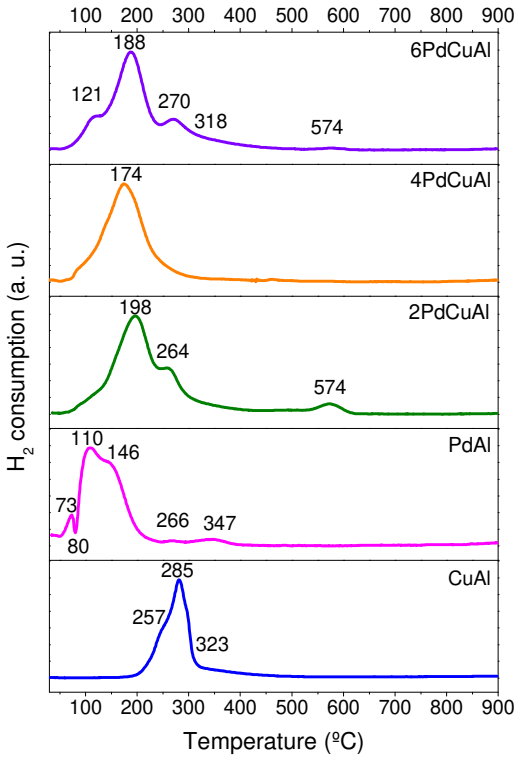

Fig. 2. TPR profiles of the mono- and bimetallic catalysts (calcined samples).

The TPR profiles of the mono- and bimetallic catalysts are presented in **Fig. 2**. **Table 1** shows the H/M ratio, defined as the ratio between the number of moles of atomic hydrogen consumed and number of moles of metal present in the samples and measured by ICP-OES (**Table 1**). The reduction profile of the monometallic CuAl catalyst shows three peaks at 257, 285 and 320°C. The results demonstrate the presence of two different types of Cu species or CuO with

two different particle size distributions, which show the TPR peaks at 257 and 285°C, as previously reported for Cu catalysts with metal loadings superior to 5 wt.% [40,41]. In agreement with previous work [42], the broad shoulder at 320 °C corresponds to the reduction of Cu_2O, which requires higher temperatures. This result agrees with the presence of both CuO and Cu_2O detected by XRD (**Fig. 1**) in the CuAl catalyst. The H/M value of 2 calculated for this solid (**Table 1**) confirms the complete reduction of Cu species.

The TPR profile of the PdAl catalyst (**Fig. 2**) exhibits a low temperature peak at 73 °C of easily reducible PdO, as well as two reduction peaks at 110 and 146 °C, which correspond to the reduction of two types of the PdO species. The negative peak at 80 °C indicates the decomposition of β-PdH, which formation has been extensively reported previously [43–45]. Hydrogen consumption at higher temperatures (266 and 347°C) has been ascribed to the reduction of PdO species strongly interacting with the γ-Al_2O_3 support or the reduction of a two-dimensional (2D) PdO surface phase formed [46] during the calcination at high temperatures, responsible for the redispersion of Pd species. The extent of such redispersion has been correlated to the calcination temperature and PdO particle size. At the calcination temperature of 350 °C, smaller Pd particles exhibit spreading, whereas the biggest ones do not [46–48]. Considering the small crystallite size determined by XRD in the PdAl catalyst, the formation of the 2D PdO phase could explain the appearance of these reduction events at high temperature in our PdAl catalyst. The hydrogen consumption of this catalyst was lower than the theoretical value, which could be due to the presence of a small quantity of metallic Pd in the Pd-Cu catalyst already before the reduction, as demonstrated by XRD (**Fig. 1**).

For the PdCu bimetallic catalysts, the TPR profiles (**Fig. 2**) are substantially more complex and different than those of their monometallic counterparts. The reduction profiles of the 2PdCuAl, 4PdCuAl and 6PdCuAl catalysts show a very intense peak at 170-190°C. This peak could be attributed to the reduction of mixed Cu-Pd species. Indeed, the reduction of Cu species seems

to be facilitated by the presence of Pd in the bimetallic particles. Palladium can enhance the reduction of Cu and larger oxide ensembles [45,49]. Interestingly, the 4PdCuAl catalyst shows a single reduction peak at 174 °C. This suggests that this catalyst principally contains a single type of Cu-Pd bimetal nanoparticles. The Pd-Cu atomic ratio in this sample corresponds to the chemical composition of $PdCu_3$ alloy [50–52].

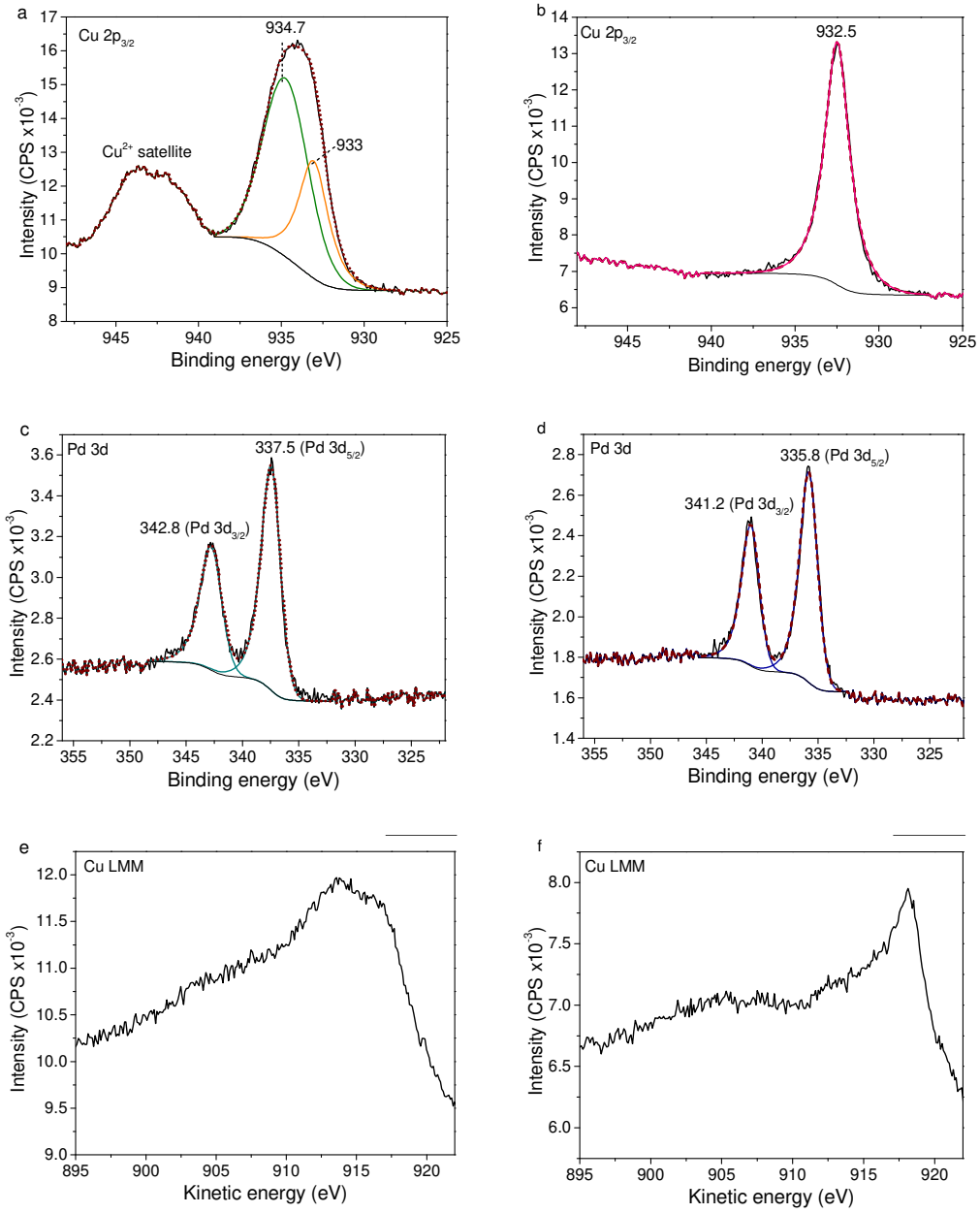

Fig. 3. Cu 3p3/2, Pd 3d and Cu LMM levels XPS spectra of the 2PdCuAl catalyst before (a, c, e) and after (b, d, f) reduction treatment under H_2 at 350 °C.

In addition to the peak at 170-190°C, the 6PdCuAl sample with higher Pd content displays a shoulder at 121°C, which can be attributed to the reduction of PdO species, while the 2PdCuAl sample with the lower Pd content and higher Cu/Pd ratio shows a high temperature peak at 264 °C, which can be probably assigned to the reduction of the CuO species.

Table 2. Binding energies of Pd $3d_{5/2}$ and Cu $2p_{3/2}$ core levels, Cu LMM Auger kinetic energy, modified Auger parameter (α') and surface atomic ratios of the mono-and bimetallic catalysts before and after reduction treatment. The suffix -R refers to the reduced samples.

Catalyst	**Pd $3d_{5/2}$ (eV)**	**Cu $2p_{3/2}$ (eV)**	**α'**	**Pd/Cu surface atomic ratio**	**Cu/Al surface atomic ratio**	**Pd/Al surface atomic ratio**
CuAl	-	934.2 932.9		0	0.021	-
CuAl-R	-	932.3	1850.3	0	0.011	-
PdAl	336.8	-	-	-	-	0.018
PdAl-R	335.3	-	-	-	-	0.010
2PdCuAl	337.5	934.7 933.0	-	0.18	0.027	0.0058/8//
2PdCuAl-R	335.8	932.5	1850.6	0.29	0.019	0.006
4PdCuAl	337.4	934.7 932.9	-	0.32	0.028	0.009
4PdCuAl-R	335.9	932.5	1850.4	0.32	0.017	0.006
6PdCuAl	336.8	933.8 933.0	-	0.28	0.021	0.008
6PdCuAl-R	335.3	932.1	1850.4	0.38	0.011	0.004

Consequently, this assignment is in good agreement with XRD, which suggests the formation of mainly isolated PdO and CuO particles in the 6PdCuAl and 2PdCuAl catalysts. In addition, no negative peak corresponding to the β-PdH decomposition is observed in the bimetallic samples, differently from the monometallic PdAl catalyst. According to Mendez [44] et al., this could be explained by the presence of Cu species within the Pd crystals, which could inhibit the formation of the hydride. The high temperature reduction peak at 574 °C for the 2PdCuAl and 6PdCuAl catalysts may be due to the reduction of $CuAl_2O_4$ and/or $PdAl_2O_4$ phases, formed due to the diffusion of Cu^{2+} and Pd^{2+} into the alumina lattice [53].

The relative surface distribution and oxidation state of Pd and Cu species in the mono- and bimetallic catalysts before and after reduction treatment under H_2 at 350 °C were elucidated using XPS. The obtained results are summarized in **Table 2**. The XPS spectra of the 2PdCuAl sample are presented in **Fig. 3**. The XPS spectra of other catalysts are given in **Figs S2** and **S3, ESI**. After the H_2 treatment, the XPS Pd/Cu atomic ratio is similar to the bulk chemical composition (**Table 1**). Both Pd/Al and Cu/Al atomic ratios decrease after the reduction treatment for all the studied samples, probably due to sintering of the metal species during the treatment under H_2 [54].

Identification of the Cu oxidation state by XPS is challenging due to the complexity of the Cu 2p level spectra, resulting from the shake-up satellites characteristic of Cu^{2+} species and overlapping binding energies [55,56] of Cu^+ and Cu^0. Consequently, determination of Cu oxidation state requires evaluation of both their characteristic binding energies and modified Auger parameter (α'). Before the reduction treatment, the deconvolution of the peak in the Cu $2p_{3/2}$ region indicates the presence of two different Cu species. The appearance of a shake-up satellite at ca. 10 eV higher binding energy than the main peak, confirms the presence of Cu^{2+} (**Fig. 3a**) [42], whereas the broad peak in the Cu LMM spectra (**Fig. 3e**) is indicative of the mixture of both Cu^{2+} and Cu^+ oxides [57], in good agreement with XRD and TPR results. After the H_2 treatment,

the disappearance of the Cu^{2+} satellite in the Cu $2p_{3/2}$ region suggests reduction of copper oxide (**Fig. 3b**). Note however, that the Cu LMM Auger peak (**Fig. 3f**) does not present the typical shape of pure metallic Cu^0, and the modified Auger parameter value is ~1 eV lower than that reported for metallic Cu [56]. This suggests the presence of both metallic Cu^0 and Cu^+ after the reduction treatment. However, the fraction of Cu^+ seems smaller than that of metallic copper, since the characteristic weak satellite of Cu^+, which should be located at around 8 eV above the main peak [58] has not been detected.

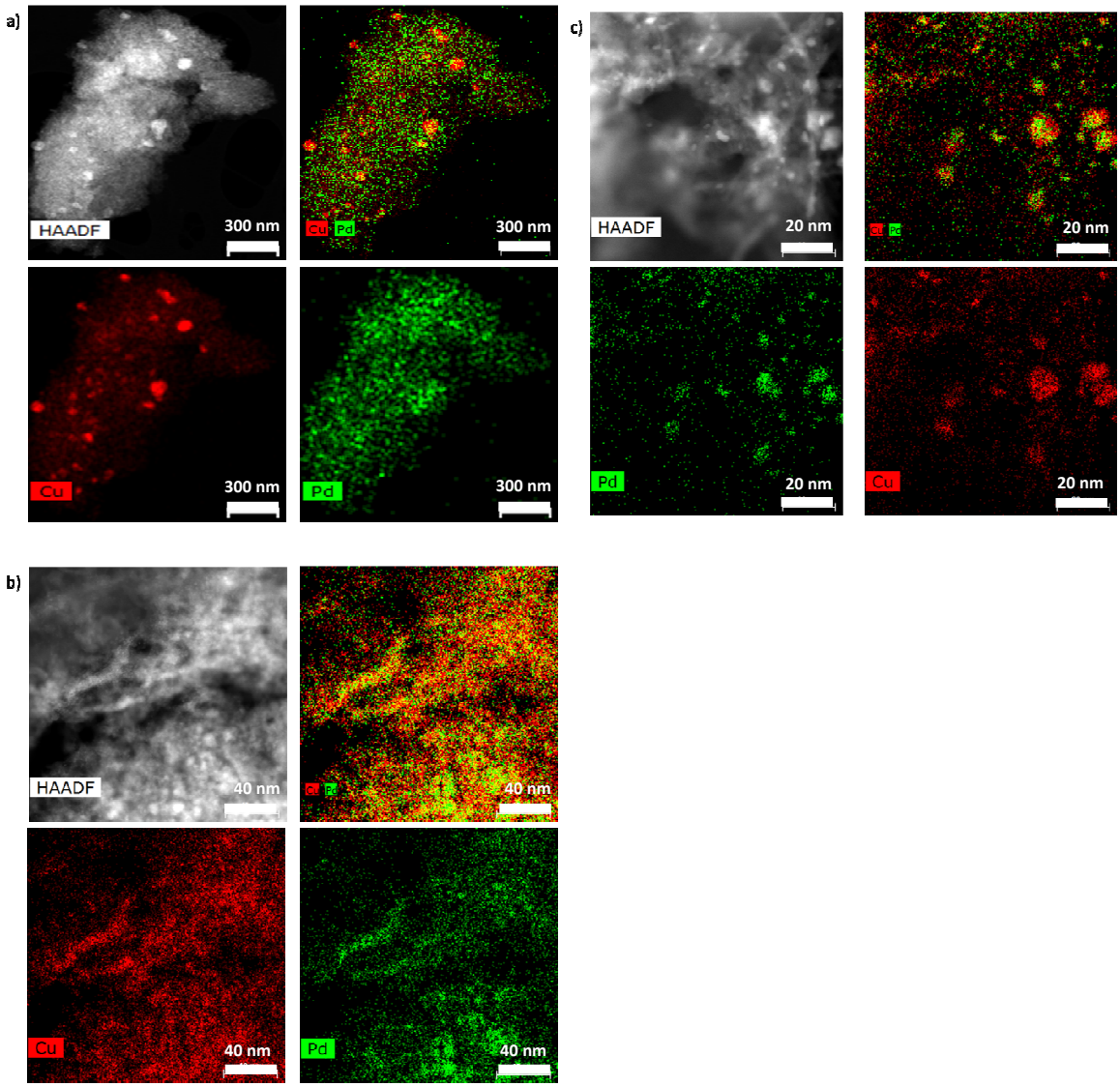

Fig. 4. HAADF-STEM micrographs and EDS mapping (Cu, Pd) of the reduced bimetallic catalysts. a) 2PdCuAl, b) 4PdCuAl, c) 6PdCuAl.

The binding energy of the Pd $3d_{5/2}$ peak indicates the presence of Pd^{2+} in all the catalysts before the reduction (**Fig. 3c**). After the reduction treatment, the peak shifts towards lower binding energy (~2 eV), which confirms the complete reduction of Pd^{2+} to Pd^0 (**Fig. 3d**). Interestingly, the Pd $3d_{5/2}$ peak in the reduced 2PdCuAl and 4PdCuAl catalysts shifts towards higher binding energy with respect to the reduced PdAl catalyst. This chemical shift may be attributed to the charge transfer and lattice strain effects derived from a strong Pd-Cu interaction, suggesting a close proximity between both metals and formation of a PdCu alloy [50,51]. On the contrary, in the 6PdCuAl catalyst with higher Pd content, the reduction results in the shift of Pd $3d_{5/2}$ XPS peaks to lower energy. This suggests the presence of isolated Pd species and a lower degree of Pd-Cu interaction, in accordance with previous observations [33]. This result also agrees with XRD, where diffraction peaks associated to isolated Pd species were detected (**Fig. 1**) and with the TPR profile of 6PdCuAl (**Fig. 2**), which shows the reduction peak attributed to the Pd species.

The particle size distribution, mean particle size and elemental composition of the reduced catalysts were evaluated by HAADF-STEM and EDS mappings (**Fig. 4**). The STEM micrograph and EDS mapping of the monometallic CuAl catalyst (**Fig. S4 a, SI**) show the presence of Cu particles with a broad particle size distribution. The Cu species present a broad particle size distribution (**Fig. 5a**) with the mean particle size of 39 nm (**Table 1**, agglomerated particles). On the contrary, Pd particles in the PdAl catalyst are uniformly dispersed in the γ-Al_2O_3 support (**Fig. 5b**), presenting a narrow particle size distribution (**Fig. 5b**) and a mean particle size of 2.8 nm. These results are in line with the crystallite sizes estimated by XRD in the calcined samples (**Fig. 1**).

The particle size and metal localization seem to be functions of catalyst composition. In the 2PdCuAl catalyst (**Fig. 4a**), both Pd-decorated Cu particles and isolated Cu particles were

distinguished. Although the mean particle size in this sample (11.4 nm) decreases with respect to the CuAl monometallic catalyst, the particle size distribution (**Fig. 5c**) is still broad.

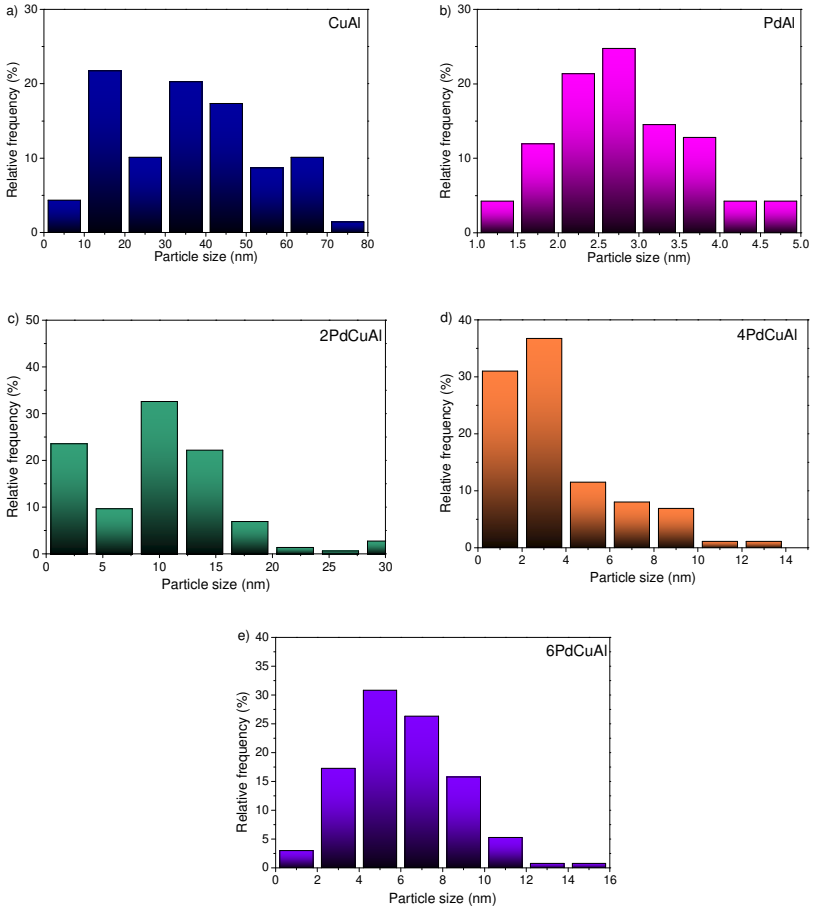

Fig. 5. Particle size distribution of the reduced mono- and bimetallic catalysts. a) CuAl, b) PdAl, c) 2PdCuAl, d) 4PdCuAl, e) 6PdCuAl

The STEM-EDS image shows the presence of both monometallic and bimetallic Cu-Pd particles. Pd seems to be in close contact with Cu particles, as previously suggested by XRD, TPR and XPS. The 4PdCuAl catalyst (**Fig. 4b**) shows a higher fraction of bimetallic nanoparticles suggesting the formation of $PdCu_3$ alloy in agreement with TPR and XPS results. Furthermore, increasing Pd content leads to a narrow particle size distribution. In the 4PdCuAl catalyst, a narrow particle size distribution (**Fig. 5d**) at 4.2 nm was observed. It seems that at higher Pd content, the sample contains a higher fraction of monometallic Pd particles. The 6PdCuAl catalyst (**Fig. 4c**) is constituted by highly dispersed nanoparticles with a narrow

particle size distribution (**Fig. 5e**). The size of bimetallic nanoparticles is around 8.5 nm, whereas very small nanoparticles of about 4-6 nm corresponding to isolated Pd particles were also detected. The quantitative information about the catalyst acidity was extracted from Py adsorption experiments combined with FTIR spectroscopy. The spectra of the hybrid catalysts reduced in hydrogen after Py adsorption at 100 °C followed by Py desorption at 150°C are presented in **Fig. 6**. The band at 1616 cm^{-1} is attributed to physisorbed Py, linked by the hydrogen bonding to the surface hydroxyl groups. The band at 1546 cm^{-1} corresponds to the C-C stretching vibrational frequency typical of pyridinium ions (PyH^+), formed as a result of Py protonation by the Brønsted acid sites [59]. The bands at 1634, 1616 and 1451 cm^{-1} correspond to υ_{8a} and υ_{19a} modes of molecularly coordinated Py (PyL), indicative of the presence of Lewis acid sites. The band at 1490 cm^{-1} indicates the mixture of both types of acid sites [33]. The Brønsted acid sites are relevant to the presence of zeolite, while the Lewis acid sites can be due to zeolite and alumina [60], which both exhibit noticeable Lewis acidity.

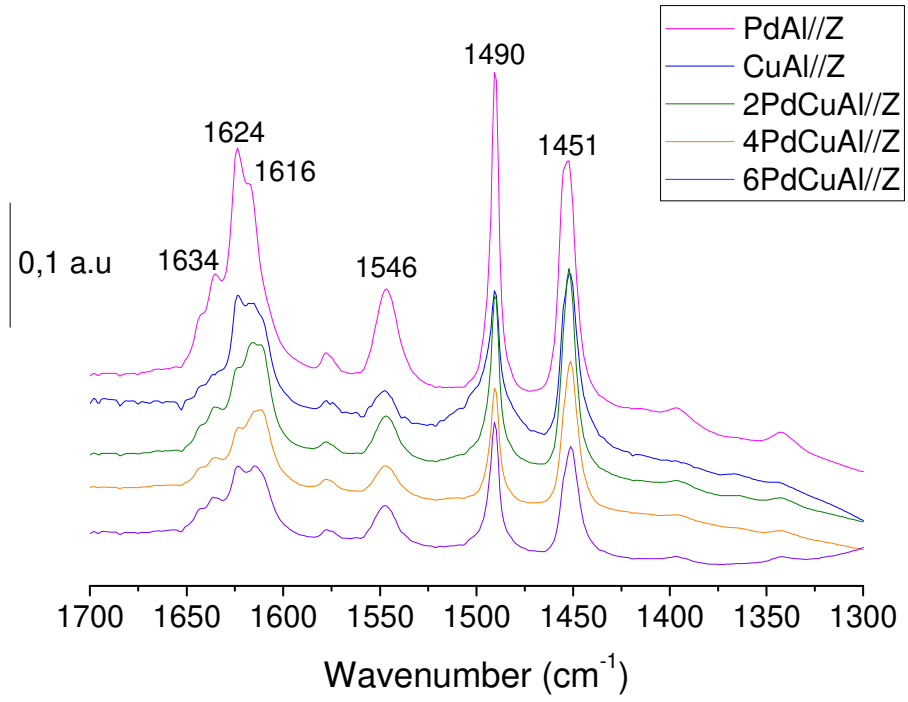

Fig. 6. FTIR spectra of the hybrid catalysts after pyridine adsorption at 100 °C and desorption at 150°C. (reduced samples).

By using the extinction coefficients (ε_B = 1.67 and ε_L= 2.22 cm/μmol) [61] for the 1546 and 1451 cm^{-1} bands, the concentrations of both types of Brønsted and Lewis acid sites were calculated. The concentrations of Brønsted acid sites in the hybrid catalysts after the Py desorption at 150 °C are shown in **Table 1**. Since the hybrid catalysts were prepared using the 5:1 mass ratio of metallic catalyst to zeolite, the concentration of Brønsted acid sites is given in **Table 1** for 1/6 g of the pure HZSM-5 zeolite. Mechanical mixing of copper metal catalysts and zeolite followed by reduction results in a much smaller number of Brønsted acid sites relative to the parent zeolite. It seems that the concentration of Brønsted acid sites is lower in the sample containing only copper (CuAl//Z), while it is slightly higher in the HZSM-5 zeolite after addition of the Pd catalyst to the zeolite. It can be suggested that some amount of Brønsted acid sites of the zeolite can be neutralized by copper during the reduction. Indeed, during the calcination and reduction, the Cu cationic species can migrate inside the zeolite. Previously, migration of copper ions in several zeolites was observed under thermal and reductive treatments [62–65] and can be also facilitated by the presence of water. Similar mechanism of deactivation of bifunctional hybrid catalysts was reported in the literature [66,67]. Note that this migration does not occur for Pd species, which can be readily reduced to the metallic state at relatively low temperature (<100°C). Metallic palladium is more stable under the reaction conditions and cannot react with the acid sites in zeolite.

3.2. Activity in the CO_2 hydrogenation

The prepared catalysts were tested in the direct DME synthesis from CO_2 at 260 °C and 20 bar. **Fig. 7** shows the evolution of CO_2 conversion over the hybrid catalysts during the 20 h of reaction. The reaction began by raising the reactor temperature from 200 to 260°C. The initial increase in CO_2 conversion is due to the hydrodynamic inertia of the high-pressure reactor (time needed for the reaction products to reach the gas-chromatograph for analysis).

The maximum CO_2 conversion under these conditions corresponding to the thermodynamic equilibrium is 20%. The catalytic tests were conducted for at least 20 h. No catalyst deactivation was detected on both monometallic and bimetallic catalysts. The CO_2 conversion values decrease as follows: CuAl//Z > 6PdCuAl//Z > PdAl//Z > 2PdCuAl//Z >> 4PdCuAl//Z (**Table 3**). High CO_2 conversion values ranging from 11 to 17% are obtained for both the monometallic and 2PdCuAl//Z and 6PdCuAl//Z bimetallic catalysts. We calculated turnover frequencies (TOF) for CO_2 hydrogenation over copper and palladium monometallic catalysts in order to evaluate the intrinsic catalytic activity of their surface sites. For the TOF calculation, the copper dispersion was estimated from copper metal particle size using the formula: $D_{Cu},\%=104/d_{Cu}$ (nm) [68], while the palladium dispersion was evaluated using the methodology developed by Fritsche [69], Montejano-Carrizales [70] and then summarized by Agostini [71].

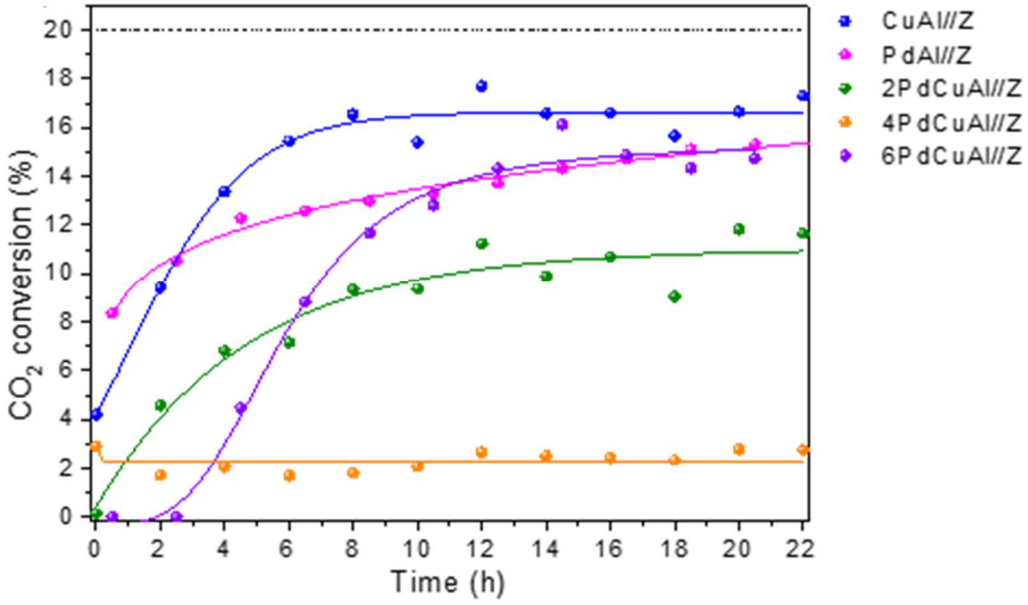

Fig. 7. CO_2 conversion over the hybrid catalysts in the direct DME synthesis reaction as a function of time on-stream. The dashed line corresponds to the equilibrium conversion in the evaluated reaction conditions (reduced samples).

The TOF value calculated for the monometallic PdAl//Z catalyst (TOF_{Pd}=0.005 s^{-1}) was almost 10 times lower than for CuAl//Z (TOF_{Cu}=0.048 s^{-1}). This suggests that, while both monometallic coper and palladium catalysts have shown high overall CO_2 hydrogenation rates,

this relatively high catalytic activity has different reasons. Over the copper monometallic catalyst, the high CO_2 hydrogenation rate arises from higher intrinsic activity of copper surface sites, whereas in the palladium monometallic counterpart, it comes from higher dispersion of palladium. At the comparable amounts of copper and palladium sites, the rate of CO_2 hydrogenation over copper-palladium bimetallic catalysts can be primarily attributed to copper surface sites, though the intrinsic activity of these copper sites seems to be noticeably affected by their interaction with palladium.

The bimetallic catalysts show significantly lower CO_2 conversions compared to the copper monometallic counterpart. Indeed, the 2PdCuAl//Z catalyst exhibits the CO_2 conversion of about slightly lower with respect to the CuAl//Z catalyst. A significant decrease in the CO_2 conversion compared to CuAl//Z is also observed over the 4PdCuAl//Z catalyst.

Table 3. Catalytic performance of metal-zeolite hybrid catalysts in CO_2 hydrogenation at steady state conditions (20% CO_2, 60% H_2 and N_2 as balance, P= 20 bar, T=260°C, GHSV=3000 cm^3/g_{cat} h.

Catalyst	**CO_2 conversion, %**	**Selectivity, %**					**DME space time yield, mmol g_{cat}^{-1} h^{-1}**
		CO	**CH_4**	**C_2H_6**	**CH_3OH**	**DME**	
CuAl//Z	17.3	91.7	0.7	0.3	3.8	3.4	0.149
PdAl//Z	15.9	32.2	65.1	0.2	2.1	0.5	0.019
2PdCuAl//Z	11.3	78.0	0	0	10.2	11.8	0.333
4PdCuAl//Z	2.7	53.8	0	0	16.4	29.8	0.200
6PdCuAl//Z	13.9	92.3	0.5	0.3	3.5	3.4	0.118

The variation of the catalytic activity of the copper-palladium bimetallic catalysts can be explained by both catalyst chemical composition and copper nanoparticle size. The low activity

of 4PdCuAl//Z catalyst could be attributed to the presence of extremely small metal particles (about 4 nm) in this sample detected by TEM. Previous report[72] indicates that the CO_2 hydrogenation to methanol is a structure-sensitive reaction. TOF over Cu-based catalysts was found [72] much lower for small copper nanoparticles and significantly increases as soon as the copper nanoparticles become larger than 8 nm. The lower activity of 4PdCuAl/Z was attributed to lower intrinsic site activity in small metallic nanoparticles. The high activity of the 6PdCuAl//Z and 2PdCuAL//Z catalysts could be explained by the increase in the bimetallic particle size up to 8 and 11.4 nm respectively. In addition, both monometallic Pd and Cu species present in these catalysts (as derived from XRD, STEM and TPR) can contribute to the reaction rate.

3.3. Selectivity to the reaction products

Direct DME synthesis from CO_2 is a multistage catalytic reaction. It proceeds via CO_2 hydrogenation to methanol (Eq. 1) followed by methane dehydration (Eq. 2). The catalyst requires therefore, a catalytic function for selective CO_2 hydrogenation, while methanol dehydration takes place on an acid catalytic component. The overall DME synthesis proceeds therefore, over a bifunctional catalyst containing both catalytic functions. The reaction selectivity can be affected by both CO_2 hydrogenation and methanol dehydration components. Let us first discuss the selectivity of CO_2 hydrogenation over the metallic component, which is the first step of DME synthesis (**Table 3**). The monometallic copper and palladium catalysts produce several reaction products such methanol, DME, methane, ethane and CO. The selectivity to CO is much higher over copper containing catalysts compared to the pallidum counterparts. CO is produced from the RWGS reaction. Because of the thermodynamic limitations, DME synthesis from CO_2 proceeds with low single pass conversion. Continuous DME production can be achieved using a recirculating process.

In addition to CO, both copper and palladium monometallic CuAl//Z and PdAl//Z catalysts produce noticeable amounts of methane and ethane, which are undesirable products of DME synthesis. Note that the production of hydrocarbons is much more significant over monometallic PdAl//Z, where the methane selectivity reached 92 %. The combined hydrocarbon selectivity (methane and ethane) was about 12% over the CuAl//Z sample. Interestingly, over the bimetallic catalysts, the selectivity of CO_2 hydrogenation to hydrocarbons has been dramatically reduced. This suggests that the methane production can be attributed to either copper or palladium monometallic sites. The contribution of the acid component to the synthesis of hydrocarbons, such as methane and ethane from CO_2 is not expected at 260°C.

For methanol synthesis from CO_2, the structure and composition of the hydrogenation catalyst plays a pivotal role, determining the nature of the reaction intermediates formed. Over the PdAl//Z monometallic catalyst, the main obtained product is CH_4, followed by CO, whereas the formation of CH_3OH and DME occurs with the combined selectivity of 4.1% (**Table 3**). This result agrees with previous studies [73], in which formation of CH_4 was favored over a 5 wt.% Pd/Al_2O_3 catalyst. At this metal loading, the fraction of Pd terrace sites forming stable CO species, which can be further hydrogenated to CH_4, is higher than at lower metal loadings, thus favoring the CH_4 formation over direct CO desorption. Although Pd alone does not favor the CH_3OH formation, its role as promoter of Cu catalysts for CH_3OH formation can be highlighted [17,74–76]. Differently from Cu, both reaction pathways can take place in the PdCu bimetallic catalysts to yield CH_3OH, depending on the Pd coverage[74].

The presence of small amount of palladium in bimetal copper-palladium catalysts is particularly beneficial for the DME synthesis. The results for the 2PdCuAl//Z catalyst demonstrate a significant increase in the oxygenated product selectivity, which reaches 100%. This sample also exhibits the higher space time yield of DME (**Table 3**). Yang[76] et al. carried

out theoretical studies to explain the reason for the methanol production enhancement in Pd-doped Cu catalysts. CH_3OH productivity in this solid seems to be enhanced due to the lower barrier for HCO hydrogenation on Pd/Cu(111) with respect to Cu(111). Over the 4PdCuAl//Z catalyst, light alkanes were neither observed. Catalyst characterization has shown the presence of copper-palladium bimetallic nanoparticles in this catalyst. Liu [75] et al. developed a theoretical model concerning CH_3OH formation on $PdCu_3$(111) surface. According to these authors, the reaction in the alloy does not occur via the formate or RWGS mechanism, but through the so-called COOH pathway. The first step of this route consists on the formation of trans-COOH from CO_2 and H. That would explain the absence of hydrocarbons over this catalyst. Finally, in the 6PdCuAl//Z catalyst, the product distribution changes with respect to its bimetallic counterparts. CO, CH_4 and C_2H_6 are formed, in addition to methanol and DME. That could be explained by the presence of a larger fraction of palladium nanoparticles in this catalyst with higher palladium content, in addition to the bimetallic copper-palladium species. These Pd nanoparticles contribute to the production of hydrocarbons. At higher Pd concentration, the production of CH_4 remains high, which is not suitable. The importance of acid sites in the second step of DME synthesis from CO_2, which is dehydration of CH_3OH, has been extensively reported in the literature[11]. In this context, the use of the H-ZSM-5 zeolite as acid catalyst has been highlighted. The ZSM-5 zeolite has comparatively greater concentration and stability of Brønsted acid sites with respect to those of γ-Al_2O_3[11,77]. The metal-zeolite hybrid catalysts prepared in this work by mechanical mixing have shown different concentrations of acid sites. Mechanical mixing of alumina supported metal catalysts and zeolite followed by reduction in hydrogen results in a considerable decrease in the concentration of the Brønsted acid sites for the hybrid catalysts (**Table 1**). Interestingly, the decrease in the concentration of Brønsted acid sites was only observed, when copper is present in the catalysts, while the monometallic palladium catalyst has exhibited the maximum amount

of Brønsted acid sites. The decrease in the concentration of Brønsted acid sites has been attributed to the migration of unreduced copper cations inside the zeolite and a partial neutralization of zeolite Brønsted sites during the temperature treatment. Previously, several techniques have detected high mobility[78,79] of copper oxidized species in zeolites. Note however, that the DME selectivity over CuAl//Z, 2PdCuAl//Z and 6PdCuAl//Z catalysts was not much affected by the amount of Brønsted acid sites (**Table 3**).

4. Conclusion

We uncovered a strong interaction between copper, palladium and zeolite in the hybrid catalysts for direct DME synthesis from carbon dioxide. Better copper reducibility and higher dispersion of the metallic phases was observed after the introduction of palladium to copper catalysts. The presence of palladium also protects copper from oxidation and slows migration of unreduced copper cationic species into zeolite during catalyst reduction, which results in lower concentration of Brønsted acid sites.

The bimetallic copper-palladium catalysts with small amount of palladium have shown higher DME yield and better DME selectivity. The copper-palladium bimetallic nanoparticles even with a small fraction of palladium suppress hydrocarbon production. The monometallic copper and palladium hybrid zeolite catalysts have shown production of noticeable amounts of methane and ethane, which are undesirable products, under the conditions of direct DME hydrocarbon formation. The DME selectivity was not much affected by the amounts of Brønsted sites in the hybrid catalysts.

Acknowledgements

The authors thank Mélanie Dubois, Olivier Gardoll and Dr Pardis Simon for the help with XRD, FTIR, TPR and XPS measurements. The authors acknowledge financial support from the European Union ("Electron to Value-Added Chemicals (E2C)" Interreg 2 Seas Project).

Conflicts of interest

There are no conflicts to declare.

References

1 D. M. D'Alessandro, B. Smit and J. R. Long, *Angew. Chemie - Int. Ed.*, 2010, **49**, 6058–6082.

2 M. Aresta, A. Dibenedetto and A. Angelini, *Chem. Rev.*, 2014, **114**, 1709–1742.

3 A. Goeppert, M. Czaun, J. P. Jones, G. K. Surya Prakash and G. A. Olah, *Chem. Soc. Rev.*, 2014, **43**, 7995–8048.

4 V. V. Ordomsky, A.-B. Dros, R. Schwiedernoch and A. Y. Khodakov, in *Nanotechnology in Catalysis*, Wiley-VCH Verlag GmbH & Co. KGaA, Weinheim, Germany, 2017, pp. 803–850.

5 S. Navarro-Jaén, M. Virginie, J. Bonin, M. Robert, R. Wojcieszak and A. Y. Khodakov, *Nat. Rev. Chem.*, 2021, **5**, 564-579.

6 J. Sun, G. Yang, Y. Yoneyama and N. Tsubaki, *ACS Catal.*, 2014, **4**, 3346–3356.

7 Z. Azizi, M. Rezaeimanesh, T. Tohidian and M. R. Rahimpour, *Chem. Eng. Process.*, 2014, **82**, 150–172.

8 N. Mota, E. Millán Ordoñez, B. Pawelec, J. L. G. Fierro and R. M. Navarro, *Catalysts*, 2021, **11**, 411.

9 C. Mevawala, Y. Jiang and D. Bhattacharyya, *Appl. Energy*, 2017, **204**, 163–180.

10 C. Mevawala, Y. Jiang and D. Bhattacharyya, *Appl. Energy*, 2019, **238**, 119–134.

11 A. Álvarez, A. Bansode, A. Urakawa, A. V. Bavykina, T. A. Wezendonk, M. Makkee, J. Gascon and F. Kapteijn, *Chem. Rev.*, 2017, **117**, 9804–9838.

12 G. Bonura, M. Cordaro, C. Cannilla, A. Mezzapica, L. Spadaro, F. Arena and F. Frusteri,

Catal. Today, 2014, **228**, 51–57.

13 R. Ciesielski, O. Shtyka, M. Zakrzewski, J. Kubicki, W. Maniukiewicz, A. Kedziora and T. P. Maniecki, *Kinet. Catal.*, 2020, **61**, 623–630.

14 X. Jiang, X. Nie, X. Wang, H. Wang, N. Koizumi, Y. Chen, X. Guo and C. Song, *J. Catal.*, 2019, **369**, 21–32.

15 J. L. G. Fierro, I. Melián-Cabrera and M. López Granados, *J. Catal.*, 2002, **210**, 285–294.

16 F. Lin, X. Jiang, N. Boreriboon, C. Song, Z. Wang and K. Cen, *Catal. Today*, , DOI:10.1016/j.cattod.2020.05.049.

17 X. Jiang, N. Koizumi, X. Guo and C. Song, *Appl. Catal. B Environ.*, 2015, **170–171**, 173–185.

18 F. Dadgar, R. Myrstad, P. Pfeifer, A. Holmen and H. J. Venvik, *Catal. Today*, 2016, **270**, 76–84.

19 G. Bonura, S. Todaro, L. Frusteri, I. Majchrzak-Kucęba, D. Wawrzyńczak, Z. Pászti, E. Tálas, A. Tompos, L. Ferenc, H. Solt, C. Cannilla and F. Frusteri, *Appl. Catal. B Environ.*, 2021, **294**, 120255.

20 X. Fan, B. Jin, S. Ren, S. Li, M. Yu and X. Liang, *AIChE J.*, , DOI:10.1002/aic.17353.

21 X. Fang, H. Jia, B. Zhang, Y. Li, Y. Wang, Y. Song, T. Du and L. Liu, *J. Environ. Chem. Eng.*, 2021, **9**, 105299.

22 H. H. Koybasi and A. K. Avci, *Catal. Today*, 2022, **383**, 133–145.

23 S. Poto, F. Gallucci and M. Fernanda Neira d'Angelo, *Fuel*, 2021, **302**, 121080.

24 H. H. Koybasi, C. Hatipoglu and A. K. Avci, *J. CO2 Util.*, 2021, **52**, 101660.

25 J. van Kampen, J. Boon, J. Vente and M. van Sint Annaland, *J. CO2 Util.*, 2020, **37**, 295–308.

26 A. Y. Khodakov, V. V. Ordomsky, A. Palčić, M. Cai, V. Subramanian, Y. Luo, V. Valtchev, S. Moldovan and O. Ersen, *Catal. Today*, 2020, **343**, 199–205.

27 M. Cai, A. Palčić, V. Subramanian, S. Moldovan, O. Ersen, V. Valtchev, V. V. Ordomsky and A. Y. Khodakov, *J. Catal.*, 2016, **338**, 227–238.

28 V. V. Ordomsky, M. Cai, V. Sushkevich, S. Moldovan, O. Ersen, C. Lancelot, V. Valtchev and A. Y. Khodakov, *Appl. Catal. A Gen.*, 2014, **486**, 266–275.

29 D. Masih, S. Rohani, J. N. Kondo and T. Tatsumi, *Appl. Catal. B Environ.*, 2017, **217**, 247–255.

30 V. Vishwanathan, K.-W. Jun, J.-W. Kim and H.-S. Roh, *Appl. Catal. A Gen.*, 2004, **276**, 251–255.

31 C. Jia, J. Gao, Y. Dai, J. Zhang and Y. Yang, *J. Energy Chem.*, 2016, **25**, 1027–1037.

32 S. Ren, W. R. Shoemaker, X. Wang, Z. Shang, N. Klinghoffer, S. Li, M. Yu, X. He, T. A. White and X. Liang, *Fuel*, 2019, **239**, 1125–1133.

33 A. S. Al-Dughaither and H. de Lasa, *Ind. Eng. Chem. Res.*, 2014, **53**, 15303–15316.

34 K. A. Cychosz, R. Guillet-Nicolas, J. García-Martínez and M. Thommes, *Chem. Soc. Rev.*, 2017, **46**, 389–414.

35 K. Okumura, R. Yoshimoto, S. Yokota, K. Kato, . HajimeTanida, T. Uruga and M. Niwa, *Phys. Scr.*, 2005, 816.

36 R. Pina-Zapardiel, I. Montero, A. Esteban-Cubillo, J. S. Moya, W. D. Kaplan, T. Paramasivam and C. Pecharromán, *J. Nanoparticle Res.*, 2011, **13**, 5239–5249.

37 H. Li, T. Yang, Y. Jiang, S. Chen, Y. He, J. Feng and D. Li, *J. Catal.*, 2020, **385**, 313–323.

38 N. Toshima and Y. Wang, *Adv. Mater.*, 1994, **6**, 245–247.

39 Y. Mun, S. Lee, A. Cho, S. Kim, J. W. Han and J. Lee, *Appl. Catal. B Environ.*, 2019, **246**, 82–88.

40 F. E. López-Suárez, A. Bueno-López and M. J. Illán-Gómez., *Appl. Catal. B Environ.*, 2008, **84**, 651–658.

41 G. V. Sagar, P. V. R. Rao, C. S. Srikanth and K. V. R. Chary, *J. Phys. Chem. B*, 2006, **110**, 13881–13888.

42 J. Batista, A. Pintar, D. Mandrino, M. Jenko and V. Martin, *Appl. Catal. A Gen.*, 2001, **206**, 113–124.

43 G. Chen, W.-T. Chou and C. Yeh, *Appl. Catal.*, 1983, **8**, 389–397.

44 C. M. Mendez, H. Olivero, D. E. Damiani and M. A. Volpe, *Appl. Catal. B Environ.*, 2008, **84**, 156–161.

45 A. N. Ardila, M. A. Sánchez-Castillo, T. A. Zepeda, A. L. Villa and G. A. Fuentes, *Appl. Catal. B Environ.*, 2017, **219**, 658–671.

46 H. Lieske and J. Völter, *J. Phys. Chem.*, 1985, **89**, 1841–1842.

47 N. S. Babu, N. Lingaiah, R. Gopinath, P. S. Sankar Reddy and P. S. Sai Prasad, *J. Phys. Chem. C*, 2007, **111**, 6447–6453.

48 J. J. Chen and E. Ruckenstein, *J. Phys. Chem.*, 1981, **85**, 1606–1612.

49 J. Sá and H. Vinek, *Appl. Catal. B Environ.*, 2005, **57**, 247–256.

50 J. Petró, T. Mallát, S. Szabó and F. Hange, *J. Electroanal. Chem.*, 1984, **160**, 289–297.

51 P. R. Subramanian and D. E. Laughlin, *J. Phase Equilibria*, 1991, **12**, 231–243.

52 J. Liu, Q. Ke and X. Chen, *J. Mater. Sci.*, 2021, **56**, 3790–3803.

53 I. S. M. Lock, S. S. M. Lock, D. V. N. Vo and B. Abdullah, *Chem. Eng. Trans.*, 2017, **57**, 343–348.

54 E. B. Fox, A. F. Lee, K. Wilson and C. Song, *Top. Catal.*, 2008, **49**, 89–96.

55 R. Castillo, S. Navarro-Jaén, F. Romero-Sarria, V. Pérez-Dieste, C. Escudero, M. Á. Centeno, M. Daturi and J. A. Odriozola, *J. Phys. Chem. C*, 2020, **124**, 19046–19056.

56 M. C. Biesinger, *Surf. Interface Anal.*, 2017, **49**, 1325–1334.

57 J. Stiedl, S. Green, T. Chassé and K. Rebner, *Appl. Surf. Sci.*, 2019, **486**, 354–361.

58 A. M. Venezia, L. F. Liotta, G. Deganello, Z. Schay and L. Guczi, *J. Catal.*, 1999, **182**, 449–455.

59 R. Buzzoni, S. Bordiga, G. Ricchiardi, G. Spoto and A. Zecchina, *J. Phys. Chem.*, 1995, **99**, 11937–11951.

60 X. Liu and R. E. Truitt, *J. Am. Chem. Soc.*, 1997, **119**, 9856–9860.

61 C. . Qin, G; Zheng, L; Xie, Y; Wu, *J. Catal.*, 1985, **95**, 609–612.

62 Y. Ma, X. Wu, S. Cheng, L. Cao, L. Liu, Y. Xu, J. Liu, R. Ran, Z. Si and D. Weng, *Appl. Catal. A Gen.*, 2020, **602**, 117650.

63 C. W. Andersen, E. Borfecchia, M. Bremholm, M. R. V. Jørgensen, P. N. R.

Vennestrøm, C. Lamberti, L. F. Lundegaard and B. B. Iversen, *Angew. Chemie Int. Ed.*, 2017, **56**, 10367–10372.

64 L. Yao, X. Shen, Y. Pan and Z. Peng, *Energy & Fuels*, 2020, **34**, 8635–8643.

65 H. Jiang, B. Guan, H. Lin and Z. Huang, *Fuel*, 2019, **255**, 115587.

66 J. L. Weber, N. A. Krans, J. P. Hofmann, E. J. M. Hensen, J. Zecevic, P. E. de Jongh and K. P. de Jong, *Catal. Today*, 2020, **342**, 161–166.

67 C. H. Mejía, D. M. A. Verbart and K. P. de Jong, *Catal. Today*, 2021, **369**, 77–87.

68 F. Arena, F.; Barbera, K.; Italiano, G.; Bonura, G.; Spadaro, L.; Frusteri, *J. Catal.*, 2007, **249**, 185–194.

69 H.-G. Fritsche and R. E. Benfield, *Zeitschrift für Phys. D Atoms, Mol. Clust.*, 1993, **26**, 15–17.

70 J. M. Montejano-Carrizales, F. Aguilera-Granja and J. L. Morán-López, *Nanostructured Mater.*, 1997, **8**, 269–287.

71 G. Agostini, R. Pellegrini, G. Leofanti, L. Bertinetti, S. Bertarione, E. Groppo, A. Zecchina and C. Lamberti, *J. Phys. Chem. C*, 2009, **113**, 10485–10492.

72 R. van den Berg, G. Prieto, G. Korpershoek, L. I. van der Wal, A. J. van Bunningen, S. Lægsgaard-Jørgensen, P. E. de Jongh and K. P. de Jong, *Nat. Commun.*, 2016, **7**, 13057.

73 J. H. Kwak, L. Kovarik and J. Szanyi, *ACS Catal.*, 2013, **3**, 2449–2455.

74 L. Liu, F. Fan, Z. Jiang, X. Gao, J. Wei and T. Fang, The Journal of Physical Chemistry C. 2017, **121**, 26287-26299

75 L. Liu, H. Yao, Z. Jiang and T. Fang, *Appl. Surf. Sci.*, 2018, **451**, 333–345.

76 Y. Yang, M. G. White and P. Liu, *J. Phys. Chem. C*, 2012, **116**, 248–256.

77 E. Topsoe, N.; Pedersen, K.; Derouane, *J. Catal.*, 1981, **70**, 41–52.

78 A. V. Kucherov and A. A. Slinkin, *Zeolites*, 1986, **6**, 175–180.

79 G. Turnes Palomino, P. Fisicaro, S. Bordiga, A. Zecchina, E. Giamello and C. Lamberti, *J. Phys. Chem. B*, 2000, **104**, 4064–4073.